Journal of Molecular Structure xxx (xxxx) 132656

Contents lists available at ScienceDirect

Journal of Molecular Structure

journal homepage: www.elsevier.com/locate/molstruc

Vibrational spectra and molecular docking studies of bergapten isolated from *Melicopedenhamii* leaves as anti-breast cancer agents

Bessy Mary Philip [a], Jerin Susan John [b], Shyni V [b], Tintu K Kuruvilla [b], Tressia Alias Princy Paulose [a], D. Sajan [b,*]

[a] Department of Chemistry, Bishop Moore College, Mavelikara, Alappuzha, Kerala 690110, India
[b] Centre for Advanced Functional Materials, Department of Physics, Bishop Moore College, Mavelikara, Alappuzha, Kerala 690110, India

ARTICLE INFO

Article history:
Received 25 November 2021
Received in revised form 15 February 2022
Accepted 17 February 2022

Keywords:
Bergapten
Vibrational analysis
NBO
QTAIM
Drug likeness
Molecular docking

ABSTRACT

This paper highlights the notable bioactivity and pharmaceutical significance of the natural furocoumarin viz. Bergapten (BG), extracted from the medicinal plant *Melicopedenhamii*. The equilibrium geometry, chemical reactivity and Natural Bond Orbital analysis to understand the charge transfer interactions of BG have been carried out aided by density functional theoretical calculations at the B3LYP/6–311 + +G(d,p) level. Vibrational spectral analysis of the extracted Bergapten, brings to light the vibrational wavenumbers and intensities of the compound. The analysis of the electron density of HOMO and LUMO gives an idea of the delocalization in the molecule and the low value of the energy gap aids in electron transport and thereby bioactivity of the molecule. Molecular docking studies which reveal the best binding sites with target proteins, particularly its inhibiting activity against carcinoma type proteins, manifest Bergapten as a promising agent for breast cancer therapy.

1. Introduction

Despite the recent advances in diagnostics and treatment, breast cancer continues to be the leading reasons of female death worldwide and the second most common cancer reported in women [1]. Over the last few years, advances in breast cancer biology has aided the development of medications targeted precisely at tumorigenesis-related molecular pathways. There are numerous issues with current chemical treatment agents which demands drugs which are effective and at the same time ensure safe treatment routes to improve clinical outcomes [2–4]. Natural compounds such as coumarins [5], isoflavones [6], and curcuminoids [7] have been demonstrated to have a significant impact on breast cancer treatment and prevention. Theoccurrence of the benzopyrone platform in the structure of coumarins gives them a wide range of biological features [8,9]. The chemical structure and physicochemical features of the coumarin scaffolds heterocyclic ring, which allow facile binding to various target proteins, are primarily responsible for its biopharmacological effects. The aromatic, planar, and lipophilic nature of the 2H-chromen-2-one ring allows it to interact with a variety of biological analogues. In addition, the coumarin's lactone group allows it to form strong polar interactions, such as hydrogen bonds, and to acylate protein targets [10]. Several analyses have recently been stated on the efficacy of coumarin derivatives in curing breast cancer, with a focus on VEGFR-2 kinase [11–13]. Furocoumarins also carry remarkable pharmacological properties, including antibacterial [14,15], anti-platelet aggregation [16] and anti-leukemia activity [17]. Moreover, furocoumarins can enhance the endurance of exposure to solar radiation [14]. Various natural 5,6,7- trioxygenated coumarins exhibit proficiency to trigger cell differentiation in human leukemia U-937 cells [18]. The focus of this research is to analyze the molecular structure, electronic properties, vibrational spectra, and molecular docking of the natural furocoumarin, bergapten (BG), extracted from the medicinal plant *Melicopedenhamii*.

2. Experimental methods

2.1. Isolation of bergapten

Fresh *Melicopedenhamii* leaves (1.2 kg) were collected and shade-dried at room temperature, cut into small pieces and powdered to obtain 600 g dry leaf powder. Leaf powder (550 g) was Soxhlet-extracted with petroleum ether (18 h), and concentrated in a rotavapor to obtain 50 g pet-ether extract.

* Corresponding author.
E-mail address: drsajanbmc@gmail.com (D. Sajan).

https://doi.org/10.1016/j.molstruc.2022.132656
0022-2860/

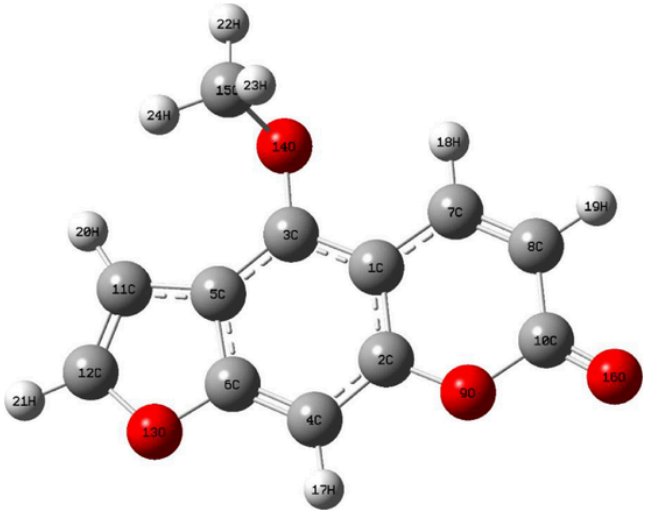

Fig. 1. Optimized structure and atom numbering of bergapten.

M. denhamii petroleum ether extract (45 g) was subjected to column chromatography (5.5 × 90 cm) over 1 kg silica gel (60–120 mesh) using hexane–chloroform (100:0 to 0:100 v/v) and chloroform–methanol (100:0 to 75:25 v/v). The collected fractions were monitored using TLC and similar fractions were pooled to obtain four major fractions. Fraction I was column-chromatographed using silica gel (60–120) in hexane-chloroform (100:0 to 30:70 v/v) to obtain 14 fractions. Fractions 7 to 13 were combined and recrystallised in hot acetone which yielded bergapten in pure form.

2.2. CharacterisationTechniques

The FT-IR spectrum of the extracted bergapten has been recorded employing a SHIMADZU infrared spectrometer by KBr pellet technique in the frequency region 4000 to 400 cm^{-1} with spectral resolution 2 cm^{-1}. FT-Raman spectrum has been recorded by means of Bruker RFS 27: standalone FT-Raman spectrometer with resolution of 2 cm^{-1}. The presence of carbon, hydrogen, nitrogen and sulfur in bergapten is determined using a CHNS analyser, model Elementar Vario EL III CHNS analyser, for powder sample weighing 7.23 mg. Optical transmittance of the solid material has been measured using JASCO V-570 UV/VIS/NIR spectrometer and NMR spectrum using R32 Perkin Elmer NMR spectrometer with DMSO as internal standard. The fluorescence spectrum has been recorded on Jobin Yvon Fluorolog 3–11 spectrofluorimeter in DMSO at different concentrations.

2.3. Computational details

Theoretical structural parameters and vibrational fundamental modes of bergapten (BG) monomer and dimer are computed using density functional theory (DFT) method with the aid of Gaussian'09 package [20]. The potential energy surface (PES) of the bergapten monomer to obtain the global minimum and local minima energy conformations at the B3LYP method with 6–311 + + G(d,p) basis set was used for the structural optimization and the computation of vibrational wavenumbers [21]. The dimer was created by separating two global minimum energy conformations of bergapten to look into hydrogen bonding via the carbonyl groups of the monomers with the furan ring. NBO calculation is executed using the program NBO 3.1 [22] and is employed to comprehend inter- and intra-molecular delocalization or hyperconjugation. Vibrational assignments using potential energy distribution (PED) is performed with MOLVIB – 7.0 program formulated by Sundius [24,25] and the scaling of the force field is performed according to the scaled quantum mechanical force field (SQMFF) procedure [26]. Electronic properties are determined by TD-DFT approach, taking solvent effect into consideration [27–29]. Molecular electrostatic potential (MEP) surface has been mapped for predicting the sites for electrophilic and nucleophilic attack as well as hydrogen-bonding interactions [30–32]. To access its biological activity, molecular docking analysis of BG is done using the software AutoDockTools 1.5.6 [33].

3. Results and discussion

3.1. NMR analysis

Nuclear magnetic resonance (NMR) spectrum of BG has been analysed to verify the existence of various types of protons and carbons. 1H NMR spectrum of BG is shown in supplementary Fig. S1. A singlet at 4.216 ppm suggests the presence of methoxy hydrogen (H24, H22, H23) in the compound. Two doublets at 6.167–6.191 ppm and 8.173–8.197 ppm were appeared for 19H & 18H protons of Coumarin. The 19H proton have involved the hydrogen bonding interaction. The 18H proton doesn't involve in any type of hydrogen bonding but the proton is surrounded by hydrogen bonded molecules. In the benzofuran moiety, the α furan proton (21H) appeared as a doublet at 7.163–7.167 ppm. The deshielded chemical shift value observed is due to hydrogen bonding with oxygen atom. The β furan proton (20H)

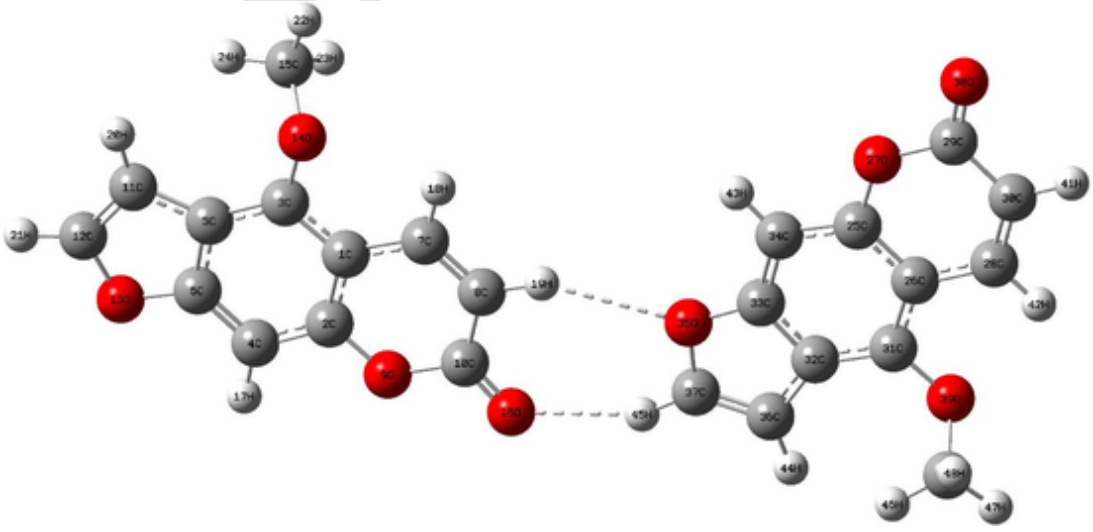

Fig. 2. Optimized structure of bergapten dimer.

Table 1
Comparison of experimental and theoretical structural parameters of bergapten.

Bonds	Bond lengths (Å)		Angles	Bond angles (°)		Angles	Dihedral angles (°)					
	Theoretical	XRD Data					Theoretical		XRD Data			
	Monomer	dimer					Monomer	dimer			Monomer	dimer
C_1—C_2	1.42	1.46	1.39	C_5—O_{15}—C_{16}	116.3	116.4	116.3	C_6—C_5—O_{15}—C_{16}	135.2	130.2	126.6	
C_3—C_4	1.44	1.35	1.42	C_2—C_1—C_3	119.7	119.8	119.4	C_2—O_9—C_{10}—O_{16}	179.8	179.6	179.7	
C_9—O_{10}	1.37	1.36	1.383	C_2—C_1—C_7	117.4	117.6	117.4	C_3—C_1—C_2—O_9	−179.9	−179.6	−178.3	
C_7=C_8	1.38	1.38	1.325	C_3-C_1-C_7	122.9	123.2	123.2	C_7-C_1-C_2-C_4	−179.7	−178.5	−178.3	
C_{12}=C_{13}	1.35	1.35	1.386	C_1-C_2-C_4	122.7	122.9	123.7	C_7-C_1-C_2-O_9	0.5	0.9	1.1	
C_2=C_3	1.35	1.35	1.34	C_1.C_2-O_9	120.6	120.9	120.1	C_2-C_1-C_3-O_{14}	−177.6	−177.5	−178.0	
C_{31}=C_{32}	–	1.38	–	C_4 -C_2-O_9	116.7	116.9	116.2	C_3-C_1-C_7-C_8	−179.9	−176.5	−177.4	
C_{26}=C_{27}	–	1.35	–	C_1 -C_3 -C_5	119.0	119.3	119.4	C_7-C_1-C_3-C_5	178.7	178.6	177.6	
H_{45}···O_{16}	–	2.29		C_1 -C_3–0_{14}	118.3	118.6	119.4	C_3-C_5-C_6-O_{13}	−179.2	−179.1	−179.6	
H_{22}···O_{15}	2.027	2.101		C_5 -C_3-O_{14}	122.6	122.6	123.2	C_1-C_2-C_4-C_6	0.7	0.9	0.6	
H_{23}···O_{15}	2.086	2.086		C_2-C_4-C_6	115.4	115.6	114.2	O_9-C_2-C_4-C_6	−179.6	179.4	−178.7	
H_{24}···O_{15}	2.101	2.067	–	C_2-C_4 -H_{17}	121.3	121.8	122.9	C_4-C_2-O_9-C_{10}	−179.9	179.4	−178.5	

showed a doublet at 7.682–7.688 ppm. A singlet was observed for 17H proton at 7.072 ppm. The 13C NMR spectrum shown in the supplementary Fig. S2 of the compound is also in accordance with the number of carbon atoms present.

3.2. CHNS analysis

Elemental analysis is used to determine the percentage composition of various elements in a compound. To confirm the non-inclusion of other species in the extracted BG, CHNS analysis is performed. The presence of carbon in BG is found to be 66.12% and that of hydrogen is 2.67%. The results show that BG contains the required percentage of elements.

3.3. Structural parameters comparison

The optimized structure of the BG isolated monomer and its atom numbering is shown in Fig. 1 and dimer in Fig. 2. The global minimum energy of BG dimer is −1526.34 kcal/mol and of monomer is −763.17 kcal/mol. The molecules in the dimer are bound together via intra molecular hydrogen-bonded interactions (C_{37}—H_{45}···O_{16} = 2.29 Å, C_8—H_{19}···O_{35} = 2.61 Å), apparently denoting rather a strong H-bonding [34]. Selected geometrical parameters have been compared with experimental XRD data [53] and are summarized in Table 1. The optimized geometrical parameters of BG monomer and dimer matched with XRD data by means of root mean-square-deviation (RMSD) values are shown in S2. RMSD values of BG monomer and dimer for geometrical parameters are in concurrence with XRD data. From the dihedral angles of the 4,4a-dihydro-3aH-furo [3,2-g]chromen-7(8aH)-one ring C_2—O_9—C_{10}—O_{16}, C_3—C_1—C_2—O_9, C_7—C_1—C_2—C_4, C_3—C_1—C_7—C_8, C_3—C_5—C_6—O_{13}, O_9—C_2—C_4—C_6 and C_4—C_2—O_9—C_{10} are 179.8°, 179.9°, −179.7°, −179.9°, −179.1°, −179.6° and −179.9°, respectively from theoretical calculations. The corresponding experimental parameters are 179.7°, −178.3°, −178.3°, −177.4°, −179.6°, −178.7° and −178.5°, respectively in the same order. It is clear that the skeleton of BG is planar. However, when the methoxy group is attached to the coumarin ring in a 4,4a-dihydro-3aH-furo[3,2-g]chromen-7(8aH)-one ring, the BG molecule attains a chair configuration.

The torsional angle of C_6—C_5—O_{15}—C_{16} is −116.9° theoretically and −126.8° experimentally. This makes it clear that the BG molecule has chair conformation. The bond angle of C_5—O_{15}—C_{16} for monomer and dimer are 116.3° and 116.4° and the torsional angle of C_6—C_5—O_{15}—C_{16} for monomer and dimer are 35.0° and 26.7° respectively. This makes it clear that the BG molecule in the dimer is a little bit distorted. The inter-molecular hydrogen bonding between methyl hydrogen and the connecting oxygen atom are C_{16}—H_{22}···O_{15} (monomer = 2.027 Å, dimer = 2.101 Å), C_{16}—H_{23}···O_{15} (monomer = 2.09 Å, dimer = 2.09 Å) and C_{16}—H_{24}···O_{15} (monomer = 2.10 Å, dimer = 2.07 Å). This gives evidence for the chair conformation in the monomer BG molecule and the distortion of the chair conformation in the dimer BG molecule. Moreover, the slight variation from the favourable arrangement of the X-H···Y fragment (X, Y: H, O) indicates a relatively strong hydrogen-bonded interaction. In addition, the dihedral angle between the withdrawing methyl group and the coumarin ring shows a variation of 1° due to the presence of methyl groups. In the monomer BG molecule, C—C double bond lengths in the rings viz. 1.33, 1.38 and 1.35 Å for C_2=C_3, C_7=C_8 and

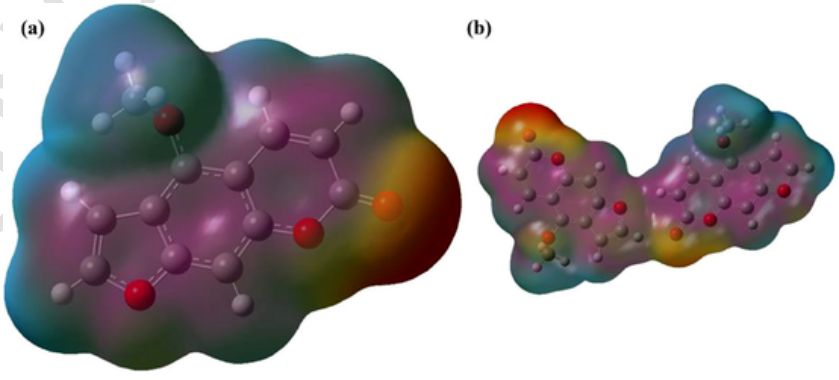

Fig. 3. Molecular electrostatic potential plots of (a) monomer (b) Dimer.

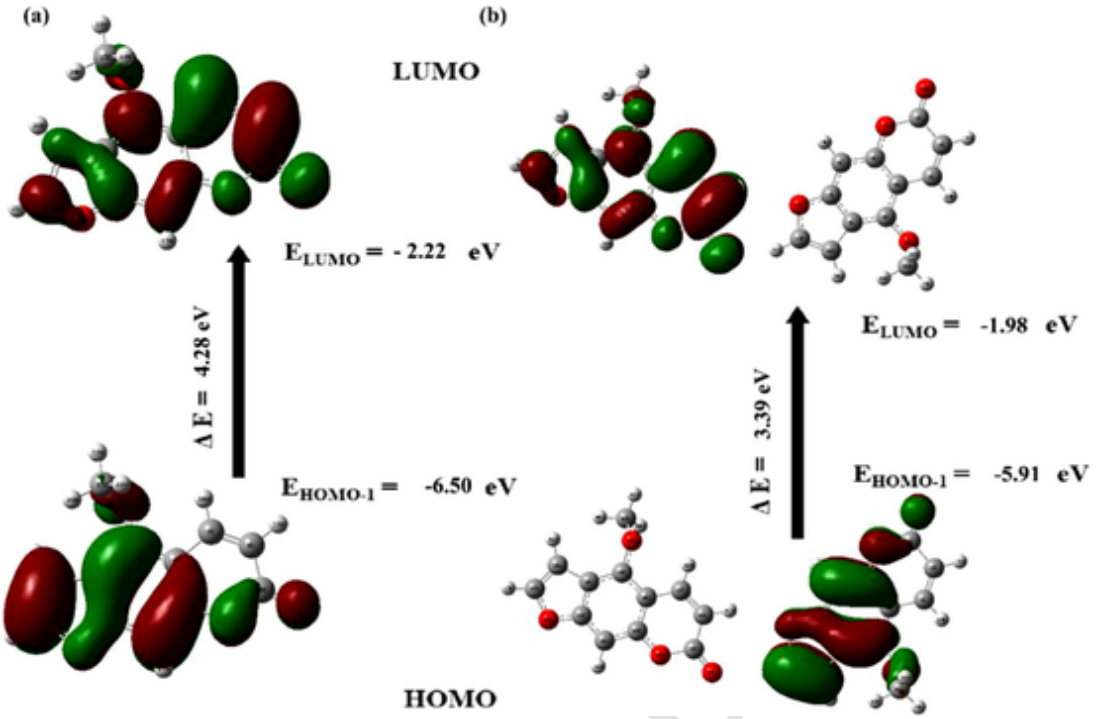

Fig. 4. Graphical representation of frontier molecular orbital of the(a) monomer (b) Dimer.

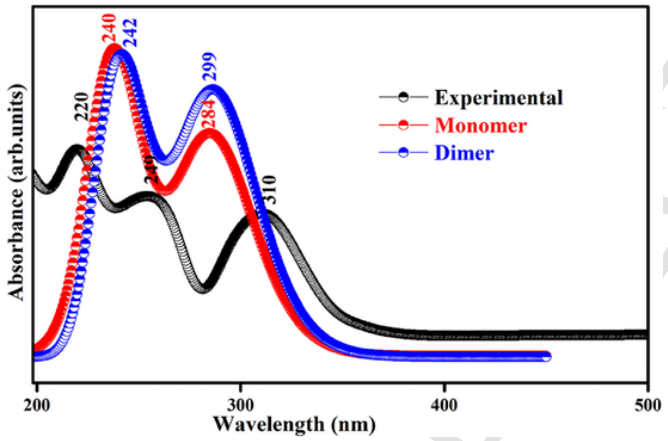

Fig. 5. UV-Visible spectra of the monomer and dimer.

C_{12}═C_{13} respectively are significantly shorter than the single bond lengths of C_1—C_2, C_9—O_{10}, O_{10}—C_1, C_7—C_{11}, C_{13}—O_{11} which are 1.44, 1.39, 1.38, 1.44 and 1.39 Å respectively. In the dimer BG molecule, double bond lengths in rings viz. 1.33, 1.38, 1.35, 1.38 and 1.35 Å for C_{28}═C_{30}, C_{34}═C_{33}, C_{36}═C_{37}, C_6═C_4, C_7═C_8 respectively are shorter than the single bond lengths of C_1—C_2, C_9—O_{10}, O_{10}—C_1, C_7—O_{11}, C_{13}—O_{11}, C_{10}—C_8, C_{10}—O_9, C_2—O_9, C_6—O_{13}, C_{12}—O_{13} which are 1.45, 1.37, 1.40, 1.36, 1.38, 1.45, 1.39, 1.37, 1.36 and 1.38 Å, respectively. C = C bond lengths in BG vary in the range from 1.32 Å to 1.39 Å. The C—C single bond length varies in dimer compared with monomer. It may be due to the charge delocalization from unit 1 to the unit 2 for stabilization. But all C = C bond lengths are nearly equal (1.38 Å) and are not affected by dimerization. However, C = C bond lengths are lengthened and C—C bond lengths are shortened in comparison with standard C = C and C—C bond lengths. In the monomer, charge has delocalized within the ring and in the case of dimer, charge has transferred from unit 1 to unit 2 and become stabilized. This has been evidenced by the inter molecular hydrogen bonding (C_{37}—H_{45}···O_{38}). In monomer and dimer, multiple bonds are shorter than single bonds between the same two elements because the additional bonding electrons attract the nuclei more strongly and pull the atoms closer together. The bond length of C = O in dimer has lengthened by ~0.01 Å. The bond elongation is due to electrostatic interactions, charge redistributions, and orbital interactions [35]. The juxtaposition between theoretical and experimental data, experimental bond lengths and bond angles are consistent with the theoretical structure, but the variations in the single and double bonds occur due to the resonant bond structure expected from this group.

3.4. Natural bond orbital (NBO) analysis

3.4.1. Donor-accepter interactions

The second-order Fock matrix has been utilized to assess the donor-acceptor interactions in the NBO analysis which provides insight into the charge transfer or delocalization of charge due to the intramolecular interaction amongst bonds. From the NBO analysis, it is observed that the C_1—C_3, C_2—C_4, C_5—C_6, C_7—C_8 and C_{11}—C_{12} bonds are having two occupancy values. The bond that occurs with the non-hydrogen bond are having both s and p hybridization, whereas the bonds that occur with the hydrogen atom are having the s hybridization for the second atom. Also, it was observed that C_1, C_2, C_3, C_4, C_5 and C_6 have low occupancy (<1.9990e) core orbital and furthermore, C_1, C_2, C_3, C_4, C_5, and C_6 have low occupancy (1.9990e) core orbitals, and the bonded atoms mentioned above have population inversion. On comparing the monomer and dimer structures for BG, the occupancy and resonance energy values for LP (2)O_{16} →σ*(C_{10}—O_9) and LP (2)O_{16}→π*(C_1—C_2) of the monomer structure in the coumarin ring are more than those in the dimer structure. Furthermore, ΔEij(2) measures the strength of the donor-acceptor interaction between orbitals. The larger the E(2) value, the more intensive is the interaction between donor and acceptor [36]. NBO occupancies and bond energy characteristics are presented in supplementary Table S4. The E (2) values corresponding to C_{37}–H_{45}···O_{16} and C_8—H_{21}…O_{35} interactions in the dimers is high with LP(O_{38}) →σ*(C_{37}—H_{21}) and LP(O_{35}) →σ*(C8-H_{19}) values of 78.63 and 73.46 kcal/mol, indicating the charge transfer interactions existing in the dimer. This intermolecular

Table 2
Calculated absorption wavelengths, electron excitation energies and oscillator strengths of BG by TD-DFT/ B3LYP/6–311 + + *G*(d,p).

Excitation	CI expansion Coefficient	Wavelength (nm)			
Calc. gas phase	Oscillator strength (f)	Excitation	CI expansion Coefficient	Wavelength (nm)	
Calc. gas phase	Oscillator strength (f)				
Monomer	Dimer				
Excited State 1	Singlet-A				
284					
240					
0.0242	*Excited State 1*	Singlet-A			
299					
242					
0.1312					
55 → 58	0.10428			112→114	0.10502
56 → 57	0.69445			112→116	0.70126
Excited State 2					
0.3655	*Excited State 2*	Singlet-A			
0.0405					
55→ 57	0.57947			112→114	0.58213
56→ 58	0.12056			112→116	0.12136
Excited State 3					
0.0059	*Excited State 3*	Singlet-A			
0.5543					
53 → 57	0.36440			112→113	0.36902
54→ 57	0.58586			112 →115	0.58847

C_{37}–H_{21}···O_{45} and C_8—H_{19}…O_{35} bond is formed by the orbital overlap between a lone pair of oxygen (O) and an antibonding orbiter (σ*) of C–H. In hydrogen bonded carbonyl group, the C = O bond is weakened. The lone pair of oxygen and antibonding orbitals of C–H are identified respectively as electron donor and acceptor NBO species. The H-bonding between LP(O) and σ*(C–H) results in charge transfer causing stabilization of the dimer species. This C–H···O intermolecular bonding increases the electron density, which leads to the elongation of the C–H bond lengths and hence lowering the corresponding stretching vibrational frequencies in dimer. Internal charge Transfer (ICT) causes the stabilization of the H-bonded systems. Hence the hydrogen bonding interaction leads to an increase in electron density of H···O antibonding orbital. The increase in the population of H···O antibonding orbital weakens the H···O bond. Thus, the properties and strength of intramolecular hydrogen bonding are explored by studying the changes in electron density near hydrogen bonds. The E(2) values corresponding to the inter-molecular hydrogen bonding in the monomer and dimer (C_{16}—H_{22}…O_{15}, C_{16}—H_{23}…O_{15} and C_{16}—H_{24}…O_{15} in monomer and C_{16}—H_{22}…O_{39}, C_{16}—H_{23}…O_{39}, C_{16}—H_{24}…O_{39}, C_{15}—H_{47}…O_{14}, C_{15}—H_{48}…O_{14}, and C_{40}—H_{48}…O_{39} in dimer) between methyl hydrogen and the connecting oxygen atom are high ($(LP(O_{15})\rightarrow\sigma^*(C_{16}—H_{22}) = 69.15$ kcal/mol, $LP(O_{15})\rightarrow\sigma^*(C_{16}—H_{23}) = 69.54$ kcal/mol and $LP(O_{15})\rightarrow\sigma^*(C_{16}—H_{24}) = 68.83$ kcal/mol on monomer) and $(LP(O_{15})\rightarrow\sigma^*(C_{16}—H_{22}) = 72.43$ kcal/mol, $LP(O_{15})\rightarrow\sigma^*(C_{16}—H_{23}) = 73.24$ kcal/mol, $LP(O_{15})\rightarrow\sigma^*(C_{16}—H_{24}) = 72.48$ kcal/mol, $LP(O_{14})\rightarrow\sigma^*(C_{15}—H_{46}) = 80.24$ kcal/mol, $LP(O_{14})\rightarrow\sigma^*(C_{15}—H_{47}) = 80.24$ kcal/mol, $LP(O_{14})\rightarrow\sigma^*(C_{15}—H_{48}) = 81.24$ kcal/mol on dimer).

3.5. Natural population analysis (NPA) and electrostatic potential (ESP)

Natural Population analysis (NPA) is a mathematical way of partitioning the wave function or electron density. Carbon atoms C_9, C_5, C_7 and C_1 in monomer and C_{29}, C_{31}, C_{25}, C_{37}, C_{10}, C_3, C_5, C_2 and C_{12} in the dimer are positive, these carbon atoms are attached with oxygen atoms. Of these, the C_1 atom on the monomer and C_1 and C_{25} atoms on the dimer have the highest positive charge, and these carbon atoms are located between the two oxygen atoms due to the delocalized charge. All other carbon atoms are negative. Also, ring carbon atoms are almost equally negative, but C_1 on monomer and C_{29}, C_{10} on the dimer is found to be positively charged. These charge variations on the carbon atoms establishes charge delocalization. Among this, C_{10} carbon atom shows a more positive charge than the C_1 atom on the monomer and dimer. Also, the C_8 carbon atom in the dimer shows a more negative charge which may be caused as a result of the intermolecular hydrogen bond (C_{37}–H_{45}···O_{16} and C_{26}—H_{19}···O_{35}). In methyl group, C_{16} on the monomer, C_{16} and C_{40} on the dimer are less negative than any other carbon atom in the BG molecule. This is due to the fact that these carbon atoms share electrons with three hydrogen atoms; whereas O_{39} and O_{38} atoms share the positive charge, showing more negative which may be due to the intramolecular hydrogen atom (on monomer C_{16}—H_{22}···O_{15}, C_{16}—H_{23}···O_{15}, C_{16}—H_{24}···O_{15} and on dimer C_{16}—H_{22}···O_{15}, C_{16}—H_{23}···O_{15}, C_{16}—H_{24}···O_{15}, C_{15}—H_{46}···O_{14}, C_{15}—H_{47}···O_{14}, and C_{15}—H_{48}···O_{14}).

Electrostatic potential (ESP) is a suitable tool in the analysis of correlation between molecular structures and the physicochemical properties of biomolecules and drugs. The ESP map for the BG molecule was carried out from the optimized molecule. The ESP of monomer and dimer have been plotted for BG molecule as shown in Fig. 3. The nuclei

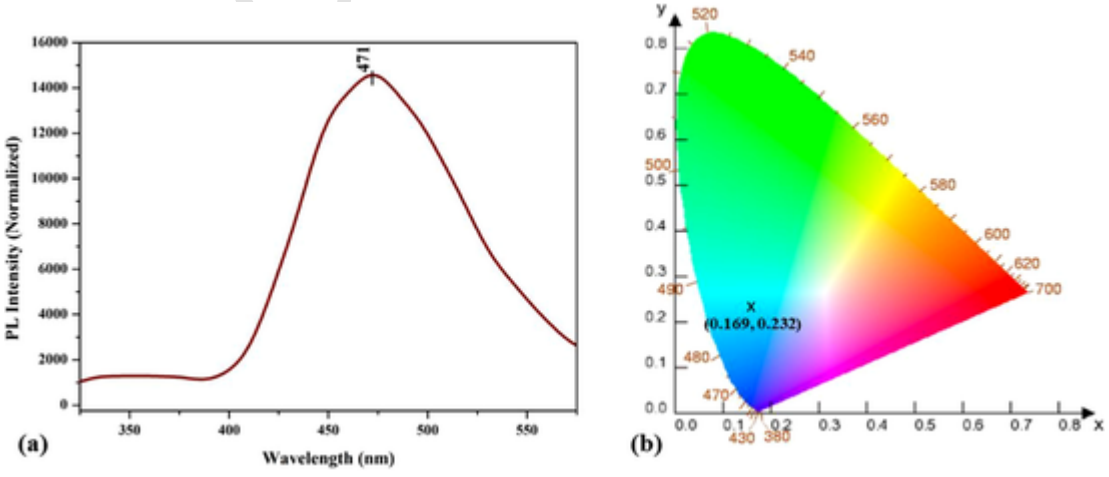

Fig. 6. (a) Fluorescence Spectrum of Bergapten (b) CIE diagram.

Table 3
Vibrational assignment of BG by NCA based on SQM force field calculations.

Observed	fundamentals/cm^{-1}	Assignment with PED (≥10%)		
ν_{IR}	ν_{Raman}	ν_{cal}		
		monomer	Dimer	
3143	3146	3149	3149	νCHI (99)
3111		3112	3111	νCHII (99)
3086	3074	3090	3089	$\nu_{IPS}CH_3$ (93)
	3012	3035	3035	$\nu_{OPS}CH_3$ (95)
2958	2958	2987	2989	$\nu_{SS}CH_3$ (89)
		1744	1747	$\nu_{AS}C{=}O$ (70), νCC (13)
1726	1715		1729	$\nu_{AS}C{=}O$ (74), νCC II (13)
	1619	1606	1605	νCHI (44), νCCII (22)
1599	1582	1595	1594	νCHII (43), νCHII (30)
	1539	1523	1527	ASYD I (38), νCCI (16), νCCIII (11), βCHI (10)
1465		1456		$CH_{3\ ASYDO}$ (98)
1365	1374	1357	1359	νCC I (73), νCCI (12)
	1295	1319	1320	νCCI (25), νCOII (16), νCOI (15), νCO III (12)
1274	1254	1266	1268	νCCIII (30), βCHII (15), νCCI (14), TD I (10)
1203	1218	1232	1233	$CH_{3\ ROCKO}$ (34), $CH_{3\ ROCK}$ (21), βCHII (17),
1147		1154	1155	$CH_{3\ ROCK}$ (57), $CH_{3\ ROCKO}$ (35),
	1131	1131	1131	$CH_{3\ ROCK}$ (57), $CH_{3\ ROCKO}$ (35),
1123		1125	1124	νCOIII (32), βCHII (12), νCOI (11), νCCII (10),
1068	1074	1061	1066	βCHII (26), νCCII (14), βCOII (13), νCOII (10),
	1032	1019	1020	τCC (43), τCC (25), R_{PUCK}II (21), R_{ASYTO} II (10),
	995	982	988	νCO(20), βCOI (10),
965			982	νCO(30), νCOII (21), βCHII (16),
	944	947	948	DEF III (23), DEFO III (23), TRI II (14),
886	898	871	884	τCC (33), τCC (32), R_{PUCK}I (10),
		821	824	R_{PUCK}II (33), τCO II(19), τRIII (10),
	792	775	777	R_{TRI} I (14), TRI II (14), τRI (11),
751		753	755	R_{PUCK}II (22), νCOII (21), DEF II (19), νCCI (18)
	643	649	648	OCCPH2 (24), νCCII (24), νCCI (10), ASYD12 (11)
584		589	590	τOC (39), τOR1 (19), τOR2 (18), τOC11C (15)
	537	572	572	νCC I (12), R_{ASYD}I (10), R_{ASYT}I (9)
521		514	516	R_{ASYDO} II (28), OCCPH2 (15), ASYD12 (12)
	498	486	487	ASYT22 (41), τOC (11), τOC (11), ASYT12 (8)

(ν)-Stretching; (ss)-Symmetric; (as)-Asymmetric; (IPS)- in plane stretching; (OPS)-out plane stretching; (ASYD)-Asymmetric deformation; (ASYDO)-Asymmetric deformation Out-of-plane; (ROCK)- Rocking; (ROCKO)- Rocking out of plane; ASYT: asymmetric torsion; ASYTO: out of plane asymmetric torsion; (β)-Bending; (DEFO)-Deformation out plane; (DEF)-Deformation; (τ)-Torsion; (PUCK)-Puckering; TRI-Trigonal deformation; PH1-Ring 1; PH2-Ring2.

and electrons produce an electrostatic potential in the space around the BG molecule which represents ESP surface. It is a very useful descriptor for the identification of various active sites of the title molecule, that can participate in electrophilic or nucleophilic reactions. The three-dimensional ESP map of the title compound is marked with different color codes between deepest red and deepest blue, ranging from −6.087 to 6.087 eV for monomer and dimer BG molecule. The value of the potential develops in the sequence red < orange < yellow < green < blue.

The blue region on the surface of the BG molecules signifies the positive value of the potential which are electron deficient areas, the red regions indicate the negative value of the map which are highly electron rich areas, whereas the zero potential of the map will be denoted by green color. The ESP map of BG molecule helps to visualize that the red and yellow region over the oxygen (O_{14} on monomer and O_{14}, O_{38} on dimer) atom represents the negative charge and are superior sites for electrophilic attack, lone pair electron oxygen which provides stabilization to the molecule enhances its bioactivity. The title molecule has more negative region around carbonyl oxygen atom while positive potential is over the methyl and hydrogen atoms. This analysis provides information about the region from where the compound can have inter and intra molecular interaction. The uniform charge distributions on the ring components protect the symmetry of the six-member ring from substituent effects. Diversely, the blue region around the hydrogen atoms on monomer and dimer in the BG molecule indulge in nucleophilic attack. This authenticates the formation of C—H···O intramolecular hydrogen bonding as demonstrated by NBO analysis.

3.6. Frontier molecular orbital and electronic absorption spectral analysis

Frontier molecular orbitals (FMOs) play a vital role in elucidation of the chemical reaction associated with the properties and energy gap of compounds. The LUMO in the monomer is localized on the coumarin ring and the carbonyl group, and the HOMO in the monomer is mainly localized on methyl phenyl acceptor ring as shown in Fig. 4(a) which can be attributed to the strong electron withdrawing nature of this group. Also, The LUMO in the dimer BG molecule is localized on the coumarin ring and the carbonyl group of the system 2, and the HOMO in the dimer BG molecule is mainly localized on methyl phenyl acceptor ring of the system 1 as shown in Fig. 4(b) which can be attributed to the strong electron withdrawing nature of this group. HOMO to LUMO transition in the monomer BG molecule implies electron density transfer from carbonyl to ring which explains a charge transfer from electron-donor groups to electron-acceptor groups through conjugated path. In the case of dimer BG molecule, electron density transfer happens from system 2 to system 1. Low frontier orbital gaps of 4.284 eV and 3.930 eV, respectively for monomer and dimer BG molecule indicates the eventual charge transfer taking place within the molecule, making it a lower band-gap energy material. The crystal has a wide transparency range, which starts in the UV region and extends up to near-infrared region through the visible region.[22] Lowering of HOMO–LUMO band gap for monomer and dimer BG molecule is essentially a significance of large stabilization of LUMO due to the strong electron-acceptor ability of electron-acceptor group.[24]

The Ionization Potential(I), Electronegativity χ (eV), Chemical hardness η (eV), Softness ζ (eV), Chemical Potential μ(eV), Electrophilicity index ψ (eV) and Dipole moment (D) has been derived from FMO's energy gap. These values for monomer are 6.445 eV, 4.303 eV, 2.142 eV, 0.467 eV, −4.303 eV, 4.320 eV, 2.495 eV in the above order. Also, these values for dimer are 6.223 eV, 4.258 eV, 1.965 eV, 0.509 eV, −4.258 eV, 4.610 eV, 2.243 eV respectively. Electrophilicity index ψ describes the biological activity [25]. The value of electrophilicity index for monomer and dimer indicates that the title compound is a biologically active compound. The high dipole moment for monomer and dimer values has confirmed that the title molecule has the dipole mo-

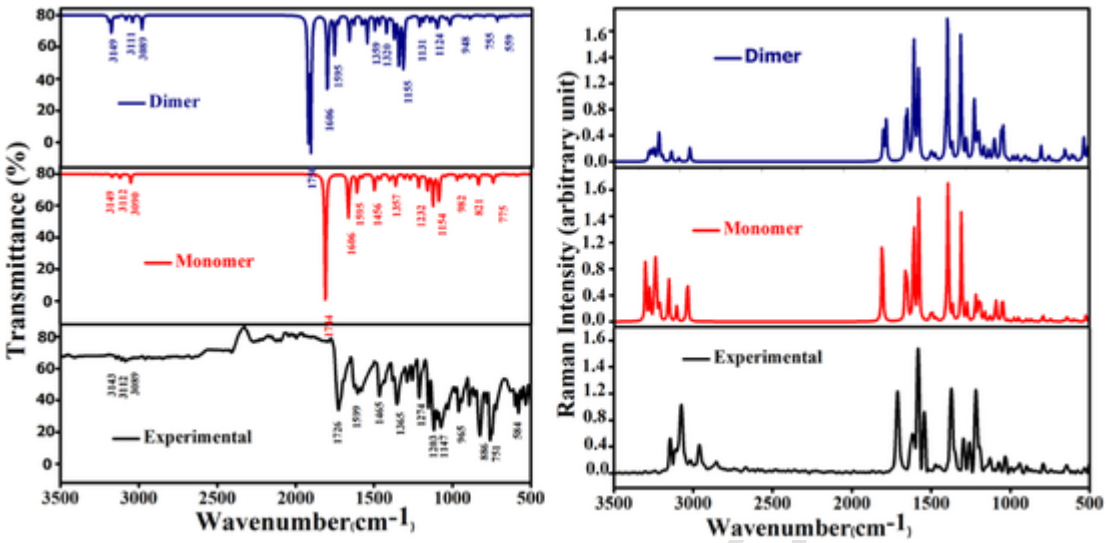

Fig. 7. Comparison of (a) FT-IR (b) FT-Raman spectra of the bergapten.

ment effects of a non-uniform distribution of charges on various atoms in a molecule. This leads to the molecular interactions involving van der Waals type dipole-dipole forces.

UV–visible absorption spectrum of BG recorded in ethanol is shown in Fig. 5. In the UV–visible region, molecules allow strong n→π* transition with high extinction coefficients. To determine the low-lying excited states, CAM-B3LYP/6–311 + + *G*(d,p) calculations have been used for monomer and dimer BG molecule. Calculated parameters are tabulated in Table 2. The maximum absorption peak (λ_{max}) predicts electronic transition at 284.35 and 240.01 nm for monomer and 299.82 and 242.05 nm for dimer, which shows good agreement with the measured experimental data at 310 nm. The very strong band in the experimental spectrum corresponds to the electronic transition from the HOMO-1 to LUMO orbitals with 96% contribution.

3.7. Photoluminescence spectra

Photoluminescence spectrum of BG is shown in Fig. 6(a) which exhibits only one emission peak located at 471 nm, which is relevant for photocatalysis. As observed in the absorption spectra, the presence of methoxybenzene in BG introduced a bathochromic shift of the photoluminescence peak. The studies of coumarin derivatives show their enhanced fluorescence property in solid state, which is easily observable by naked eye under UV irradiation.[24] Fig. 6(b) gives the CIE diagram, the co-ordinates of which for bergapten are (0.169, 0.232, and 0.599) and the color corresponding to the emission lies in the blue region. The quantum yield of the title compound is determined using Quinine sulfate as the standard with absorbance at 310 nm. The calculated quantum yield, calculated using Eq. (1) and tabulated in supplementary Table S5 is found to be less than the fluorescence standards observed.

$$Q = Q_{ref}\left(\eta^2/\eta^2_{ref}\right)(I/A)\left(A_{ref}/I_{ref}\right) \quad (1)$$

where η is the refractive index of the solvent used, which, for DMSO is 1.479, η_{ref} = 1.34 for 0.1 M H_2SO_4 and Q_{ref} = 0.54 (Quantum yield of Quinine Sulphate)

3.8. Vibrational analysis

Vibrational assignments of BG have been achieved with normal coordinate analysis (NCA). Non-redundant set of internal coordinates has been defined and used as data file for MOLVIB program while selective scaling has been included according to the scaled quantum mechanical (SQM) scheme with the RMS frequency error 8 cm^{-1}. Vibrational active relevant modes of spectral assignments with PED contributions are tabulated in Table 3 and detailed vibrational mode assignments of monomer and dimer are included in the supplementary information Table S6. Experimental FT-IR and FT Raman spectra along with the simulated spectra are shown in Fig. 7(a) and (b)for visual comparison.

3.8.1. Methoxy group vibrations

Electronic effects and intermolecular hydrogen bonding in the crystalline network alter the wavenumbers of the vibrational modes of the methoxy group in BG. Back-donation and induction effects, which are mostly induced by the presence of an oxygen atom close to the CH_3 group, can shift the band position of CH stretching and bending modes. In both IR and Raman, the vibrations of the methoxy groups appear as intense bands, although they differ significantly from the normal values of methyl groups. As previously reported [37–39], this must be owing to the electronic effect caused by the presence of oxygen atoms, which produces a variation from expected values. The back donation and the conjugation of the lone pair of oxygen with the p_z orbital of the aryl ring are two competing effects for methoxy substituted phenyl groups, whose relative weights influence the conformation dependent molecular properties [38]. The conjugation of the oxygen lone pair with the aryl p_z orbital changes during the methoxy rotation, reaching a maximum when the carbon atom of the methoxy group is in the plane of the ring. The methoxy carbon atom is 118.00º out of the ring plane in BG, indicating that methoxy group has a nearly perpendicular conformation (=90º).

Asymmetric and symmetric methyl stretching bands have been identified at 2960 and 2846 cm^{-1} respectively, in vibrational spectrum analyses on coumarin derivatives [40,41]. The stretching modes of methoxy are calculated to be 3089 cm^{-1} for asymmetric and 2989 cm^{-1} for symmetric [54]. For methoxy group, the comparable experimental values are 15 and 31 cm^{-1} lower, respectively, because to its proximity to the phenyl ring. In the IR and Raman spectra, the asymmetric and symmetric stretching modes of methoxy groups of the BG are seen as medium bands at 3086, 2958 cm^{-1} and 3074, 2958 cm^{-1}, respectively. The electronic effects of back-donation and induction due to the presence of the oxygen atom may be responsible for this decrease in wavenumber [39,41].

The CH_3 umbrella modes are also identified in IR spectrum the expected range, 1465 cm^{-1} supported by the computed values with 98% contribution of PED. The CH_3 group rocking vibrations are BG mixed vibrations. The combination of C—H in plane bend and CH_3 rock produces the medium 1203 cm^{-1} in the IR spectrum, as well as the match-

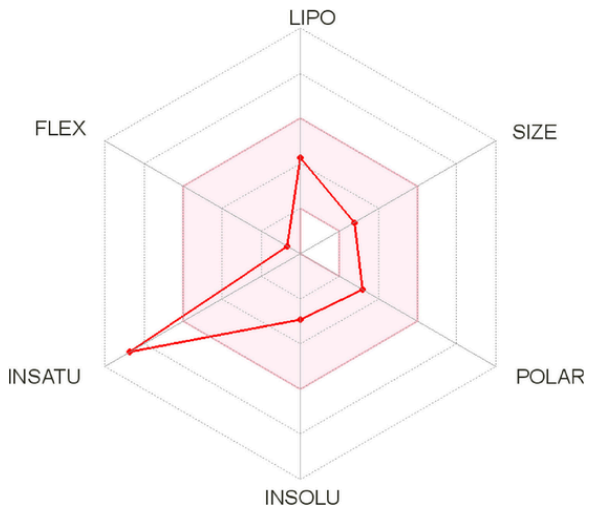

Fig. 8. Bioactivity of bergapten molecule.

ing Raman bands at 1218 cm^{-1}, in agreement with the calculated results

3.8.2. Carbonyl group vibrations

Carbonyl stretching vibrations can be observed between 1750 −1700 cm^{-1} [42,43]. The carbonyl vibration in the pyrone ring correlates to the weak IR band at 1726 cm^{-1} and the medium band at 1715 cm^{-1} in the Raman spectrum. The theoretically computed values of monomer are 1744 (70%) and dimer 1747 (70%); 1729 (74%) shows fair agreement with the experimental value. The C = O bond in the lactone portion of BG is conjugated to the double bonds C_1—C_2 and C_4—C_9. The wavenumber of carbonyl and double bond absorptions decreases when single bond character increases due to conjugation. The carbonyl vibrational wavenumber of C_{26}—O_{38} stretching in the lactone portion is decreased to varying extents due to conjugation, which is supported by NBO results also. The resonance energy for LP (2)O_{16}→σ*(C_{37}—H_{45}) is 78.63, according to the NBO analysis of donor–acceptor interactions. This is attributed to the increasing nature of the oxygen lone pair. The strong ICT connections that contribute to molecular stabilization cause these increased interaction energies, and this mechanism is significant in BG's biological activity. In the IR spectrum, the C–O stretching bands are seen as medium intensity band at 1123 cm^{-1}, whereas the corresponding computed values are observed in the same positions, at 1125 cm^{-1}. The C–O skeletal mode correspond to a weak Raman band at 995 cm^{-1}.

3.8.3. Ring vibrations

The three rings viz. the 2H-pyran ring, 5,6-Dihydro-2H-pyran-2-one ring and tetrahydrofuran ring are attached together which is known as 4,4a-dihydro-3aH-furo[3,2-g]chromen-7(8aH)-one ring (ring system). The 2H-pyran ring and 5,6-Dihydro-2H-pyran-2-one ring attached together is known as coumarin ring. Multiple bands in the 3100–3000 cm^{-1} range result from aromatic C–H stretching vibrations [41,42]. These modes appear in experimental Raman at 3241, 3144 and 3111 cm^{-1} and their counterpart in IR at 3216, 3181, 3143, 3124 and 3087 cm^{-1}. These modes contributed 89–100% of the PED, implying that these local coordinates adequately explain the C–H aromatic vibrations. The nature of the substituents in this region has no effect on the bands. The experimental and DFT-calculated wavenumbers are in fair agreement.

The aromatic C–H in-plane bending vibrations are observed as bands in the range 1290–900 cm^{-1} [41–43]. The bands at 1254 cm^{-1}, 1123 cm^{-1}, 1068 cm^{-1} in the experimental Raman spectrum and the bands at 1254 cm^{-1}, 1074 cm^{-1}in the IR spectrum are attributed to the C–H in plane bending. The strongest absorptions for the aromatic ring have also been identified in the range 1000–600 cm^{-1} due to out-of-plane C—H bending vibrations [41–43]. These are observed in the Raman spectrum at 965 cm^{-1}, 886 cm^{-1}, 751 $cm^{-1}$and in the infrared spectrum at 944 cm^{-1}, 792 cm^{-1}. The arising CH in plane and out of plane bending modes may be due to the stereo electronic hyperconjugative interactions between the axial C—H bonds in the coumarin ring. The NBO analysis (supplementaryS2) clearly shows that there is 68.26 kcal/mol involved in the σ (C_7—H_{18}) →σ*(C_8—H_{19}) stereo electronic hyperconjugative interaction and the shifting may be due to the interference between the C = C and C = O in the coumarin ring. The C–H in plane bending and C–H out of plane vibrations are coupled to the C–C–C bending modes, as revealed through PED calculations.

The stretching vibrations of the C–C ring have resulted in distinct bands in both the IR and Raman spectra, spanning the spectral range from 1610 to 1300 cm^{-1}. The ring stretching vibrations are responsible for the bands seen in the infrared and Raman spectra for coumarin derivatives at 1617, 1603, 1556, 1338, 1109, 807, and 748 cm^{-1}. The ring mode appears in the Raman spectra of BG as prominent bands at 1619 cm^{-1} and 1582 cm^{-1}. Infrared bands identified at 1599 cm^{-1} belong to ring mode, which is located on the benzene part of the molecule. The band at 1619 cm^{-1} is attributed to the mode (8a) of benzene [45]. The medium band at 1365 cm^{-1} and 1374 cm^{-1} in the infrared and Raman spectra respectively, is mostly a C–C stretching of benzene, which is also supported by PED calculations. The infrared bands observed at 886 cm^{-1} and 584 cm^{-1} for BG have been characterized as ring in-plane bending modes. According to the PED calculations, the C–C stretching vibration is coupled with the C–C–H bending modes Table 3. shows the vibrations corresponding with ring stretching, in-plane bending, and out-of-plane bending.

3.9. Biological activity

3.9.1. Predicting the bioavailability of molecules

To compute physicochemical descriptors as well as to predict ADME parameters such as pharmacokinetic properties, drug-like nature and medicinal chemistry friendliness of molecules to support drug discovery, a web tool has been used [46]. The oral bioavailability of BG is shown in the Fig. 8. The colored zone of Fig. 8 gives information about physiochemical space for oral bioavailability.

The physicochemical property such as unsaturation property has been violated. All other physicochemical properties such as, the molar refractivity, topological polar surface area, number of heavy atoms and number of aromatic heavy atoms (within the oral consumption limit) is obeyed. It has been deduced that BG molecule can be used for oral consumption in the aspects of physiochemical property. Another aspect is the affinity of a drug for a lipid environment (lipophilicity). Lipophilicity, most commonly referred to as the LogP, represents the ratio at the equilibrium of the concentration of a compound between two phases, an oil and a liquid phase [46]. It has been explained in terms of the partition coefficient (P) as Consensus Log Po/w (2.16) [47]. The Consensus Log Po/w (2.16) has been obtained from the average of the five predictions by calculating LogP in five methods. They are Log P in house physics-based method (Log Po/w (iLOGP) (2.29)), atomic and knowledge-based method (Log Po/w (XLOGP3) (1.93)), atomistic method (Log Po/w (WLOGP) (2.55)), topological method (Log Po/w (MLOGP) (1.18)) and hybrid fragmental/ topological method (Log PO/w (SILICOS-IT) (2.88)). The high value of LogP (Log $P > 1$) of BG molecule fulfills the required selectivity and potency of drugs. The solubility of BG molecule has been calculated in two methods, topological method and fragmental method. The solubility of BG molecule often requires low doses in order to reach therapeutic plasma concentrations after oral administration. Gastrointestinal absorption is high in BG4 molecule. The Blood-Brain Barrier score of BG molecule is 4.50. It lies in the moderate region. It shows that BG molecules protect against circulating toxins or pathogens that could cause brain infections, while at the same time al-

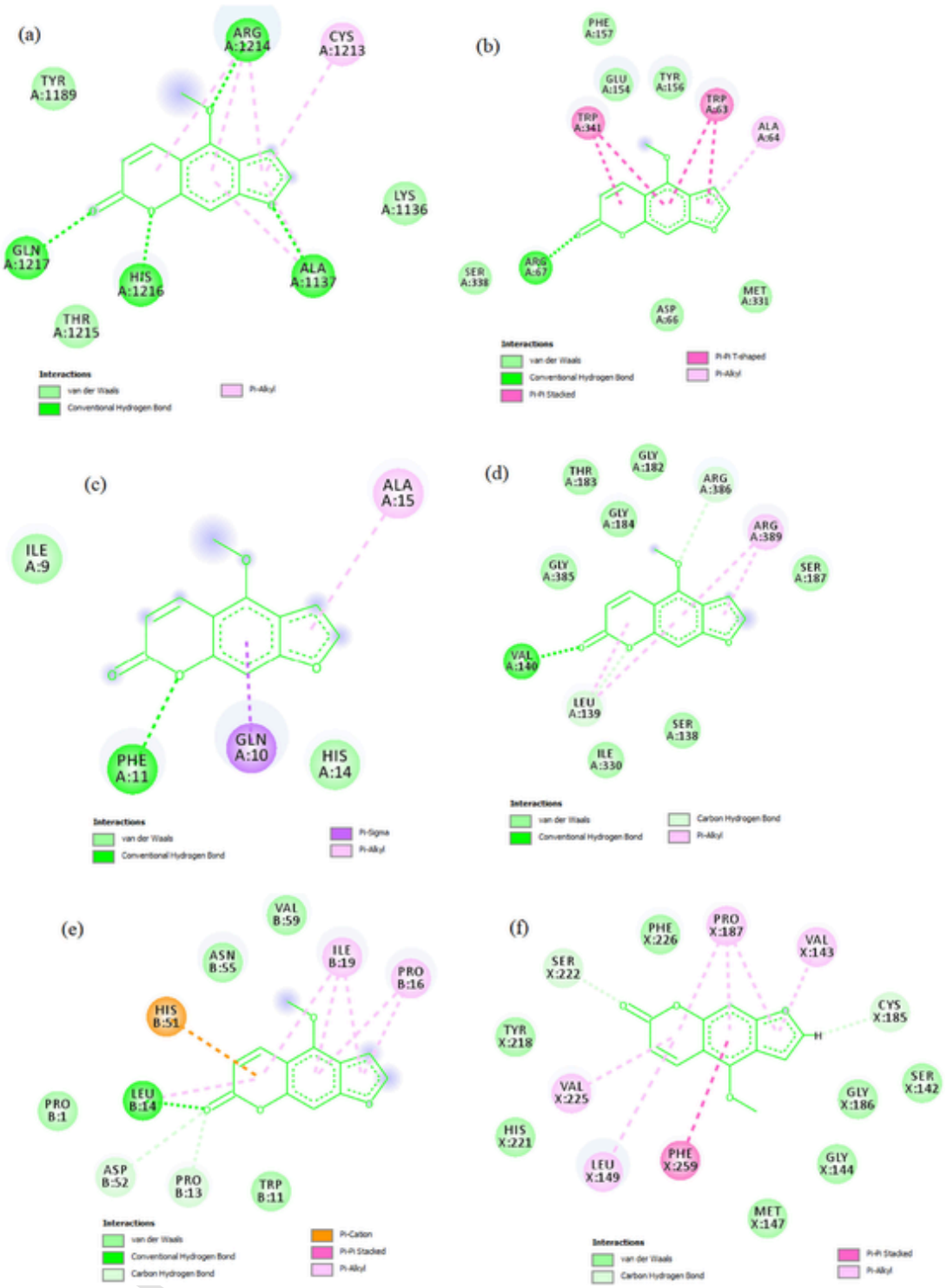

Fig. 9. Pictorial representation of possible binding sites of bergapten with the target proteins (a) 1QG3 (b) 1EM9 (c) 1MG1 (d) 6TON (e) 6L98 (f) 3HB4.

lowing vital nutrients to reach the brain. P-gp substrate, CYP2C19 inhibitor, CYP2C9 inhibitor, CYP2D6 inhibitor and CYP3A4 inhibitor effects in BG molecule confer multidrug resistance in cancer chemotherapy. Skin permeation or the rate of a chemical penetrating across the stratum corneum is 6.25 cm/s. In the case of drug likeness, BG molecule obeys Lipinski rule, Ghose rule, Veber rule, Egan rule and Muegge rule. The bioavailability score, synthetic accessibility and drug-likeness model score are 0.55, 2.90 and −0.65, respectively. The ADMET values exhibits that the BG molecule has a very good absorption in the cell.

3.9.2. *Molecular docking*

Molecular Docking is the technique employed for finding new drugs and their binding confirmation, energies and affinities with target proteins. According to the type of cell, cancer types can be grouped into broader categories including carcinoma (1QG3), sarcoma (1EM9), leukemia (1MG1), lymphoma (6TON) and myeloma (6L98) [1,2]. Subject to the goal and systems of interest, computer-assisted drug discovery methodologies have been widely employed to improve the effectiveness of the drug discovery and development pipeline in drug inquiry. Molecular docking is a tool that contributes towards this devel-

opment. The discovery and characterization of multiple target proteins that regulate cell growth, differentiation, motility, and death has ushered in a new era of cancer treatment. This work concentrates on the possibility of therapeutic inhibition of the proteins viz. 1QG3 [55,56], 1EM9[57], 1MG1[58], 6TON[59] and 6L98 [60] which can provide insight into the treatment of the related types of cancer.

The title compound (ligand) BG is docked into the active sites of the proteins causing carcinoma (1QG3) [48], sarcoma (1EM9) [49]), leukaemia (1MG1) [50]), lymphoma (6TON) [51]) and myeloma (6L98) [52]). The structure of the above-mentioned cancer proteins were retrieved from the Protein Data Bank for docking analysis. To find the best-docked conformation, the least binding energy, the number of hydrogen-bonding and the estimated inhibition energy have been calculated. The Binding energy of BG molecule with (1QG3) (1EM9), (1MG1), (6TON) and (6L98) proteins are −7.56 kcal/mol, −4.76 kcal/mol, −6.23 kcal/mol, 4.61 kcal/mol and 5.14 kcal/mol, respectively. The inhibition constant of BG molecule with carcinoma, sarcoma, leukaemia, lymphoma and myeloma proteins is 323.44 mM, 256.21 mM, 296.36 mM, 248.36 mM and 284.24 mM, respectively. The binding site and binding orientations are given in the Fig. 9.

The intermolecular energy of BG molecule with carcinoma, sarcoma, leukaemia, lymphoma and myeloma proteins is −2.06 kcal/Mol, 5.32 kcal/Mol, 3.01 kcal/Mol, 3.56 kcal/Mol and 3.56 kcal/Mol, respectively. The hydrogen bond interactions of ligand-carcinoma protein are C_1—O_{14}···H (2.0139 Å), C_9—O_{10}···O (1.6918 Å), C_5—O_{15}···H (2.1126 Å) and C_7—O_{11}···H (2.3731 Å) with the amino acids GLN A, HIS A, ARG A and ALA A, respectively. The hydrogen bond interactions of ligand-sarcoma protein are C_1—O_{14}…O (2.3930 Å), C_9—O_{10}···H (1.7423 Å), C_5—O_{15}···O (2.0501 Å) and C_7—O_{11}···H (2.0320 Å) with the amino acids LEU B, TRP A, LEU B and LEU B, respectively. The hydrogen bond interactions of ligand-leukaemia protein are C_1—O_{14}···H (2.2878 Å) and C_9—O_{10}···H (2.1260 Å), with the amino acids ARG A. The hydrogen bond interactions of ligand-lymphoma protein are C_1—O_{14}···H (2.2609 Å), C_5—O_{15}···O (2.2609 Å), C_1—O_{14}···H (2.0510 Å), C_7—O_{11}···H (2.2981 Å) and C_7—O_{11}···O (1.0192 Å) with the amino acids THR A, THR A, PHE A, HIS A and PHE A, respectively. The hydrogen bond interactions of ligand-myeloma protein are C_1—O_{14}···H (1.7022 Å), C_5—O_{15}···O (1.9683 Å), C_5—O_{15}···O (2.2153 Å) and C_9—O_{10}···H (1.1.8484 Å) with the amino acids VAL A, THR A, ARG A and ARG A respectively. The results point out that carcinoma type protein(1QG3) has more affinity towards the BG molecule than sarcoma, leukaemia, lymphoma and myeloma type cancer proteins. For this reason, docking study of BG molecule has been carried out against breast cancer (carcinoma type cancer) protein 3HB4. The binding energy, inhibition constant and intermolecular energy of BG molecule with breast cancer(3HB4) proteins are −7.66 kcal/mol, 330.32 mM and −2.04 kcal/Mol, respectively. The hydrogen bond interactions of ligand-breast cancer protein are C_1—O_{14}···H (2.3349 Å), C_9—O_{10}···O (1.8521 Å), C_7—O_{11}···H (2.2384 Å) and C_5—O_{15}···O (1.8527 Å) with the amino acids TYR X, PHE X, VAL X and GLY X, respectively. The above results exhibit inhibitory activity of BG molecule against breast cancer cells [61–63].

4. Conclusion

The compound bergapten was isolated from *Melicopedenhamii leaves* and the structural parameters were analyzed computationally using Gaussian '09 program software. Chemical reactivity of molecule based on DFT for rationalizing the interaction between different molecular systems has also been studied. Natural Bond Orbital analysis supports the presence of charge transfer interactions in the molecule. A complete vibrational analysis of BG was performed on the basis of the SQM force field obtained by DFT calculation. The wavenumbers proposed by PED calculations are in concurrence with the observed wavenumbers. Lowering of HOMO–LUMO energy gap value suggests the possibility of intra-molecular charge transfer in the molecule making it a suitable bioactive compound. Molecular docking with target proteins reveal the inhibiting action of BG against carcinoma type proteins. The potential therapeutic abilities of BG has been manifested in this study and the autodocking studies are useful in the development of new drugs based on this compound or some analogs.

Uncited references

[19,23,44,57,58,59].

CRediT authorship contribution statement

Bessy Mary Philip: Investigation, Conceptualization, Writing – original draft. **Jerin Susan John:** Methodology, Data curation, Validation, Writing – original draft, Writing – review & editing. **Shyni V:** Formal analysis, Data curation. **Tintu K Kuruvilla:** Data curation, Validation. **Tressia Alias Princy Paulose:** Supervision. **D. Sajan:** Writing – review & editing, Funding acquisition, Supervision.

Declaration of Competing Interest

The authors declare that they have no known competing financial interests or personal relationships that could have appeared to influence the work reported in this paper.

Supplementary materials

Supplementary material associated with this article can be found, in the online version, at doi:10.1016/j.molstruc.2022.132656.

References

[1] L.S. Rebecca, M. D.Kimberly, J. Ahmedin, Cancer statistics, 2018, CA Cancer J. Clin. 68 (1) (2018) 7–30.
[2] E.Y. Ahmed, N.A. Abdel Latif, M.F. El-Mansy, W.S. Elserwy, O.M. Abdelhafez, VEGFR-2 inhibiting effect and molecular modeling of newly synthesized coumarin derivatives as anti-breast cancer agents, Bioorg. Med. Chem. 28 (5) (2020) 115328.
[3] S. Balani, L.V. Nguyen, C.J. Eaves, Modeling the process of human tumorigenesis, Nat. Commun. 8 (1) (2017) 2041, -1723.
[4] S. Setrerrahmane, H. Xu, Tumor-related interleukins: old validated targets for new anti-cancer drug development, Mol. Cancer 16 (1) (2017) 1476–4598.
[5] M.A. Musa, J.S. Cooperwood, M.O.F. Khan, Areviewofcoumarinderivativesinpha r-macotherapyofbreastcancer, Curr. Med. Chem. 26 (15) (2008) 2664–2679.
[6] F.F. Zhang, et al., Dietary isoflavone intake and all-cause mortality in breast cancer survivors: the breast cancer family registry, Cancer 123 (11) (2017) 2070–2079, 2017.
[7] K. Parveen, K. Almesh, K.S. Prashanth, A.M. Nitin, S.J. Vinayak, C. B.Chandana, B.G. Anil, Curcumin as an adjuvant to breast cancer treatment, anti-cancer agents, Med. Chem. 15 (5) (2015) 647–656.
[8] K. Venkata Sairam, B.M. Gurupadayya, R.S. Chandan, D.K. Nagesha, B. Vishwanathan, A review on chemical profile of coumarins and their therapeutic role in the treatment of cancer, Curr. Drug Deliv. 13 (2) (2016) 186–201.
[9] D. Srikrishna, C. Godugu, P.K. Dubey, A review on pharmacological properties of coumarins, Mini Rev. Med. Chem. 18 (2) (2018) 113–141.
[10] A. Stefanachi, F. Leonetti, L. Pisani, M. Catto, A. Carotti, Coumarin: a natural, privileged and versatile scaffold for bioactive compounds molecules, 23(2) (2018) 250.
[11] M.M. Ghorab, M.S. Alsaid, A.M. Soliman, F.A. Ragab, VEGFR-2 inhibitors and apoptosis inducers: synthesis and molecular design of new benzo [g] quinazolin bearing benzenesulfonamide moiety, J. Enzyme Inhib. Med. Chem. 32 (1) (2017) 893–907.
[12] R.Z. Batran, D.H. Dawood, S.A. El-Seginy, M.M. Ali, T.J. Maher, K.S. Gugnani, A.N. Rondon-Ortiz, New coumarin derivatives as anti-breast and anti-cervical cancer agents targeting VEGFR-2 and p38α MAPK, Arch. Pharm. 350 (9) (2017) 1700064.
[13] T.K. Mohamed, R.Z. Batran, S.A. Elseginy, M.M. Ali, A.E. Mahmoud, Synthesis, anticancer effect and molecular modeling of new thiazolylpyrazolyl coumarin derivatives targeting VEGFR-2 kinase and inducing cell cycle arrest and apoptosis, Bioorg. Chem. 85 (1) (2019) 253–273.
[14] B.R. Scott, M.A. Pathak, G.R. Mohn, Molecular and genetic basis of furocoumarin reactions, Mutat. Res. 39 (1) (1976) 29–74.
[15] S. Omar, L.A. Eriksson, Interaction and photobinding between 8-methoxypsoralen and thymine, Chem. Phys. Lett. 471 (1–3) (2009) 128–132.
[16] P.S. Song, K.J. Tapley, Photochemistry and photobiology of paoralens, Photochem. Photobiol. 29 (6) (1979) 1177–1197.

[17] W.D. Spielmann HP, T.J. Dwyer, J.E. Hearst, Solution structures of psoralen monoadducted and cross-linked DNA oligomers by NMR spectroscopy and restrained molecular dynamics, Biochemistry 34 (40) (1995) 12937–12953.
[18] O.M. Abdel Hafez, K.M. Amin, N.A. Abdel-Latif, T.K. Mohamed, E.Y. Ahmed, T. Maher, Synthesis and antitumor activity of some new xanthotoxin derivatives, Eur. J. Med. Chem. 44 (7) (2009) 2967–2974.
[19] S. George, R. Venkataraman, S. Baby, Melicodenine I, a new quinolinone alkaloid from *Melicopedenhamii* leaves, Nat. Prod. Res. 31 (8) (2017) 890–895.
[20] M.J. Frisch, G.W. Trucks, H.B. Schlegel, et al. Gaussian 09,RevisionA02. Wallingford CT: GaussianInc; 2010.
[21] S. Saravanan, V. Balachandran, Quantum mechanical study and spectroscopic (FT-IR, FT-Raman, UV-Visible) study, potential energy surface scan, Fukui function analysis and HOMO-LUMO analysis of 3-tert-butyl-4-methoxyphenol by DFT methods, Spectrochim. Acta A Mol. Biomol. Spectrosc. 130 (15) (2014) 604–620.
[22] E.D. Glendening, A.E. Reed, J.E. Carpenter, F. Weinhold NBO Version 3.1.TCI.University of Wisconsin: GaussianInc; 1998.
[23] S.K. Wolff, D.J. Grimwood, J.J. Mckinnon, M.J. Turner, D. Jayathilaka, M. A.Spackman. Crystal Explorer Version 3.1. University of Western Australia, 2012.
[24] T. Sundius, MOLVIB-A Flexible Program for Force Field Calculations, J. Mol. Struct. (1) (1990) 321–326.
[25] T. Sundius, Scaling of ab initio force fields by MOLVIB, Vib. Spectrosc. 29 (2) (2002) 89–95.
[26] P. Pulay, G. Fogarasi, G. Pongor, E.J. Boggs, A. Vargha, Combination of theoretical ab initio and experimental information to obtain reliable harmonic force constants. Scaled quantum mechanical (SQM) force fields for glyoxal, acrolein, butadiene,formaldehyde, and ethylene, J. Am. Chem. Soc. 105 (24) (1983) 7037–7047.
[27] P. Pulay, G. Fogarasi, F. Pang, J.E. Boggs, Systematic ab initio gradient calculation of molecular geometries, force constants, and dipole moment derivatives, J. Am.Chem. Soc. 101 (10) (1979) 2550–2560.
[28] W. Kohn, A.D. Becke, G. R, Parr density functional theory of electronic structure, J.Phys. Chem. 100 (31) (1996) 12974–12980.
[29] R.G. Parr, R.G. Pearson, Absolute hardness: companion parameter to absolute electronegativity, J. Am. Chem. Soc. 1059 (26) (1983) 7512–7516.
[30] J.F. Luque, M.J. Lopez, M. Orozco, Perspective on Electrostatic interactions of a solutewith a continuum. A direct utilization of ab initio molecular potentials for the previsionof solvent effects, Theor. Chem. Acc. 103 (3) (2000) 343–345.
[31] P. Politzer, S.J. Murray, The fundamental nature and role of the electrostatic potential inatoms and molecules, Theor. Chem. Acc. 108 (3) (2022) 2002134–2002142.
[32] P. Politzer, F. Abu-awwad, Regular article A comparative analysis of Hartree-Fock and Kohn-Sham orbital energies, Theor. Chem. Acc. 99 (2) (2022) 199883–199887.
[33] G.M. Morris, R. Huey, W. Lindstrom, et al., AutoDock4 and AutoDockTools4: automated docking with selective receptor flexibility, J. Comput. Chem. 30 (16) (2009) 2785–2791.
[34] G.R. Desiraju, T. Steiner, The Weak Hydrogen Bond, Oxford University Press, New York, 1999.
[35] X. Li, L. Liu, H.B. Schlegel, J. Am. Chem. Soc. 124 (32) (2002) 9639–9647.
[36] I.V. Alabugin, M. Manoharan, S. Peabody, F. Weinhold, Electronic basis of improper hydrogen bonding: a subtle balance of hyperconjugation and rehybridization, J. Am. Chem. Soc. 125 (19) (2022) 5973–5987, 23.
[37] M. Rumi, G. Zerbi, J. Mol. Struct. 509 (1999) 11.
[38] G.M. Anderson, P.A. Kollman, L.N. Domelsmith, K.N. Houk, J. Am. Chem. Soc. 101 (1979) 2344.
[39] M. Tommasini, C. Castiglioni, M. Del Zoppo, G. Zerbi, J. Mol. Struct. 169 (1999) 480–481.
[40] M. Gussoni, C. Castiglioni, J. Mol. Struct. 521 (2000) 1.
[41] B. Smith, Infrared Spectral Interpretation–A Systematic Approach, CRC Press, NewYork, 1999.
[42] V. Arjunan, R. Santhanam, S. Sakiladevi, M.K. Marchewka, S. Mohan, J. Mol. Struct. 1037 (2013) 305–316.
[43] F.M. Moghaddam, B.K. Foroushani, J. Mol. Struct. 1065 (2014) 235–240.
[44] R.M. Silverstein, G.C. Basseler, C. Morill, Spectroscopic Identification of OrganicCompounds, Wiley, New York, 1981.
[45] G. Varsanyi, Vibrational Spectra of Benzene Derivatives, 1st ed., New York: Academic Press, 1969.
[46] A. Daina, O. Michielin, V. Zoete, SwissADME: a free web tool to evaluate pharmacokinetics, drug-likeness and medicinal chemistry friendliness of small molecules, Sci. Rep. 7 (1) (2017) 1–13.
[47] T. Bohnert and C. Prakash, "ADME profiling in drug discovery and development: an overview," Encyclopedia of Drug Metabolism and Interactions, (2012) 1–12.
[48] J.M. de Pereda, Crystal structure of a tandem pair of fibronectin type III domains from the cytoplasmic tail of integrin alpha 6beta 4, EMBO J. 18 (15) (1999) 4087–4095.
[49] R.L. Kingston, T. Fitzon-Ostendorp, E.Z. Eisenmesser, G.W. Schatz, V.M. Vogt, C.B. Post, and M.G. Rossmann, "Rous sarcoma virus capsid protein: c-terminal domain," 88(13) (2014) 7170–7177.
[50] C.W. Tindale, The authority of testimony, ProtoSociology 13 (1) (1999) 96–116.
[51] B.R. Bellenie, K.M.J. Cheung, A. Varela, O.A. Pierrat, G.W. Collie, G.M. Box, M.D. Bright, S. Gowan, A. Hayes, M.J. Rodrigues, K.N. Shetty, M. Carter, O.A. Davis, A.T. Henley, P. Innocenti, L.D. Johnson, M. Liu, S. de Klerk, Y.V.L. Bihan, M.G. Lloyd, P.C. McAndrew, E. Shehu, R. Talbot, H.L. Woodward, R. Burke, V. Kirkin, R.L.M. van Montfort, F.I. Raynaud, O.W. Rossanese, S. Hoelder, Achieving *in vivo* target depletion through the discovery and optimization of benzimidazolone BCL6 degraders, J. Med. Chem. 63 (8) (2020) 4047–4068.
[52] H. Matsumura, Y. Furukawa, T. Nakagaki, C. Furutani, S. Osanai, K. Noguchi, M. Odaka, M. Yohda, H. Ohtani, Y. Michishita, Y. Kawabata, A. Kitabayashi, S. Ikeda, M. Nara, A. Komatsuda, N. Takahashi, H. Wakui, Multiple myeloma–associated Ig light chain crystalline cast nephropathy, Kidney Int. Rep. 5 (9) (2020) 1595–1602.
[53] A.K. Bauri, S. Foro, Q.N.N. Do, Crystal structure of bergapten: a photomutagenic and photobiologically active furanocoumarin, Acta Cryst. E 72 (8) (2016) 1194–1196.
[54] A. Shumaila, M. Rehman, J. Zulfiqar, S. Najam, M.H. Asim, F. Abid, Compatibility analysis of bergapten with different pharmaceutical excipients used in nanostructured lipid carriers, Pak. J. Pharm. Sci. 32 (6) (2019) 2879–2885.
[55] E...E. El-Sawy, M.S. Rady, H.M. Shalby, A.B. Ahmed, H.M. Abo-Salem, Synthesis and molecular docking of novel non-cytotoxic anti-angiogenic sulfonyl coumarin derivatives against hepatocellular carcinoma cells *in vitro*, J. App. Pharm. Sci. 7 (2017) 049–066.
[56] M. Neelgundmath, K.R. Dinesh, et al., Novel synthetic coumarins that targets NF-κB in Hepatocellular carcinoma, Bioorg. Med. Chem. Lett. 25 (4) (2015) 893–897.
[57] T.H. Stefanova, N.J. Nikolova, R.A. Toshkova, H.O. Neychev, Antitumor and immunomodulatory effect of coumarin and 7-hydroxycoumarin against Sarcoma 180 in mice, J. Exp. Ther. Oncol. 6 (2) (2007) 107–115.
[58] B.Y. Wang, Y.C. Lin, Y.T. Lai, J.Y. Ou, W.W. Chang, C.C. Chu, Targeted photo responsive carbazole–coumarin and drug conjugates for efficient combination therapy in leukemia cancer cells, Bioorg. Chem. 100 (2020) 103904.
[59] M. Patel, N. Pandey, J. Timaniya, P. Parikh, A. Chauhan, N. Jain, K. Patel, Coumarin–carbazole based functionalized pyrazolines: synthesis, characterization, anticancer investigation and molecular docking, RSC Adv. 11 (44) (2021) 27627–27644.
[60] T.K. Mohamed, R.Z. Batran, S.A. Elseginy, M.M. Ali, A.E. Mahmoud, Synthesis, anticancer effect and molecular modelling of new thiazolyl pyrazolyl coumarin derivatives targeting VEGFR-2 kinase and inducing cell cycle arrest and apoptosis, Bioorg. Chem. 85 (2019) 253–273.
[61] J. Vikas J, D. Sakshi, G. Kunal, K. Sankalp, K.M. Darpan, P. Shalmali, B. Anjali, B. Agraj, Screening of phytochemicals as potential inhibitors of breast cancer using structure based multitargeted molecular docking analysis, Phytomed. Plus 2 (2) (2022) 10022.
[62] D.K. Yadav, S. Kumar, H.S. Saloni, M. Kim, P. Sharma, S. Misra, F. Khan, Molecular docking, QSAR and ADMET studies of withanolide analogs against breast cancer, Drug Des. Dev. Ther. 11 (2017) 1859, -187.
[63] V. Shah, J. Bhaliya, G.M. Patel, In silico docking and ADME study of deketene curcumin derivatives (DKC) as an aromatase inhibitor or antagonist to the estrogen-alpha positive receptor (Erα+): potent application of breast cancer, Struct. Chem. (2022).